An Experimental Kinestatic Comparison between Continuum Manipulators with Structural Variations

Kai Xu*, *Member, IEEE*, Minxiao Fu and Jiangran Zhao, *Student Member, IEEE*

Abstract—**Continuum manipulators attract a lot of interests due to their advantageous properties, such as distal dexterity, design compactness, intrinsic compliance for safe interaction with unstructured environments. However, these manipulators sometimes suffer from the lack of enough stiffness while applied in surgical robotic systems. This paper presents an experimental kinestatic comparison between three continuum manipulators, aiming at revealing how structural variations could alter the manipulators' stiffness properties. These variations not only include modifying the arrangements of elastic components, but also include integrating a passive rigid kinematic chain to form a hybrid continuum-rigid manipulator. Results of this paper could contribute to the development of design guidelines for realizing desired stiffness properties of a continuum or hybrid manipulator.**

I. INTRODUCTION

CONTINUUM manipulators, mentioned in [1], received a lot of attentions in the past decades due to their advantageous properties, such as intrinsic compliance, distal dexterity, etc. They have been applied in a variety of manipulation applications in unstructured settings [2-5].

Continuum manipulators also have a great potential for medical applications because of their intrinsic soft interaction with human anatomy and the design compactness achieved by the dual roles of their elastic parts as both structural components and motion output members. They have been used as active cannulae [6, 7], catheters [8-10], endoscopes (such as arthroscope [11], colonoscope [12]), and surgical manipulators [13-15].

Some continuum manipulators were found especially useful to form a compact yet dexterous and versatile DDU (Distal Dexterity Unit) for surgical robotic systems. For example, the continuum manipulator had 8 DoFs (Degrees of Freedom) and an outer diameter of 4.2mm in the throat MIS (Minimally Invasive Surgery) robot [13], whereas the continuum manipulator had 7 DoFs (Degrees of Freedom) and an outer diameter of 6.5mm in the IREP robot [14]. What's more, 15 DoFs for two manipulators and a vision unit were packed into a Ø12mm endoscopic robot for NOTES (Natural Orifices Transluminal Endoscopic Surgery) [15].

While applied in a DDU of a surgical robotic system, stiffness of these continuum manipulators is sometimes not high enough due to their intrinsic compliance. Insufficient stiffness could deteriorate the performance of such a DDU.

Several attempts are made by this paper, aiming at improving the stiffness of a slim and multi-DoF continuum manipulator for future applications. The attempts include the placement of additional elastic components and the integration of a passive rigid kinematic chain.

An experimental kinestatic comparison between three continuum manipulators is presented. As shown in Fig. 1, Structure-I has a simple structure and Structure-II has a highly redundant arrangement of elastic components, whereas Structure-III has a passive rigid kinematic chain integrated. In order to make the comparison fair and consistent, the three continuum manipulators all have the same outer diameter of 7 mm with an identical length of 33 mm. Results of this paper could contribute to the development of design guidelines for continuum manipulators with desired stiffness properties.
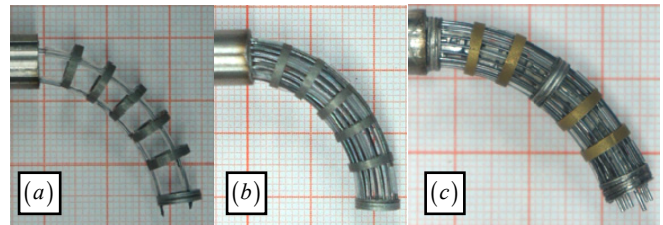

Fig. 1. Three continuum manipulators to be compared: (a) Structure-I with three elastic backbones; (b) Structure-II with a redundant arrangement of components; (c) Structure-III with a passive rigid kinematic chain integrated

Major contribution of this paper is the proposal and the experimental comparison of the approaches (use redundant elastic components and/or integrate a rigid kinematic chain) for the stiffness enhancement of continuum manipulators. The integration of a passive rigid kinematic chain opens new possibilities to design a hybrid continuum-rigid manipulator for desired stiffness properties. Minor contribution is the design and the implementation of a novel modular actuation scheme which conveniently drives all the continuum manipulators.

The paper is organized as follows. Section II presents the comparison formulation. Kinematics and statics of the to-be-compared continuum manipulators are presented in Section III. Section IV presents a novel actuation scheme and the construction of the actuation unit. Detailed experimental characterization of the continuum manipulators' kinematics and stiffness properties are presented in Section V with conclusions and future work followed in Section VI.

II. Comparison Formulation

Three continuum manipulators were compared as shown in Fig. 2. They all have the same outer diameter of 7 mm with an identical length of 33 mm. Referring to the specific designs in Fig. 2 and the generic structure in Fig. 3, Structure-I consists of three secondary backbones, an end disk, several spacer disks and a base disk. One virtual primary backbone can be identified in the center, which characterizes the shape and the length of Structure-I. The three secondary backbones are equidistant from each other and are only attached to the end disk. They can slide in the holes in the spacer disks and in the base disk. 2-DoF bending of Structure-I is realized by simultaneously pushing and pulling the secondary backbones.

When Structure-I is applied as a surgical manipulator, it is expected to handle various payloads dexterously. Dexterity of the manipulator is often affected by the bending radius of the structure and a smaller bending radius could lead to more dexterous motions. For a manipulator with a specific length, the minimal bending radius puts a limit on the diameter of the secondary backbones. For this reason, it should not be the first option to use thicker backbones to improve the stiffness of Structure-I. Structure-II is hence formed by using more secondary backbones (18 in total). A 2-DoF bending of Structure-II could also be realized by simultaneously pushing and pulling all these secondary backbones.

Stiffness properties of Structure-II could be further improved by integrating a passive rigid kinematic chain into the continuum structure to form a hybrid continuum-rigid manipulator. As shown in Fig. 2(c) and Fig. 4, a RRPRR kinematic chain is added into Structure-II to form Structure-III in order to improve the torsional rigidity. The proposal of Structure-III actually opens a wide variety of topological options for designing hybrid continuum-rigid structures with various stiffness properties.

The three structures will be actuated according to their kinematics as presented in Section III. The actuation is realized in a modular way using the actuation scheme from Section IV. Experimental comparisons between the three structures in terms of the kinematics and the stiffness properties are presented in Section V.
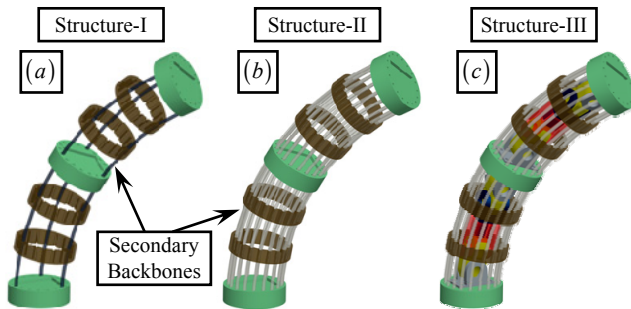

Fig. 2. CAD models of three continuum manipulators with Ø7mm outer diameters: (a) Structure-I, (b) Structure-II and (c) Structure-III

III. Nomenclature and Kinematics

This paper investigates possible means to improve the stiffness of a continuum manipulator for scenarios where high manipulation stiffness is desired. Preferably the increased stiffness will not result in a complicated kinematics model to hinder the real-time tele-operation of the manipulator.

As demonstrated in [13, 14], the surgical continuum manipulator utilized the continuum segments similar to Structure-I and the simple kinematics model facilitated the tele-operation of the surgical manipulator. The kinematics of Structure-I depends on its shape and the shape was described and experimentally verified to be close enough to a circular arc [16]. Structure-II and Structure-III are designed for improved stiffness properties. Their shapes are still assumed to be circular when their kinematics is derived. Experimental characterization in Section V will validate this assumption, showing both structures still have simple circular shapes with enhanced stiffness properties.

A. Nomenclature

Nomenclatures are defined in Table I, while the coordinate systems are defined as follows.

- *Base Disk Coordinate System* (BDS) is designated as $\{b\} \equiv \{\hat{\mathbf{x}}_b, \hat{\mathbf{y}}_b, \hat{\mathbf{z}}_b\}$. It is attached to the base disk of the continuum structure, whose XY plane coincides with the base disk and its origin is at the center. $\hat{\mathbf{x}}_b$ points from the center to the first secondary backbone while $\hat{\mathbf{z}}_b$ is normal to the base disk. Secondary backbones are numbered according to the definition of δ_i.

- *Bending Plane Coordinate System 1* (BPS1) is designated as $\{l\} \equiv \{\hat{\mathbf{x}}_l, \hat{\mathbf{y}}_l, \hat{\mathbf{z}}_l\}$ which shares its origin with $\{b\}$ and has the virtual primary backbone of the continuum structure bending in its XZ plane.

- *Bending Plane Coordinate System 2* (BPS2) is designated as $\{2\} \equiv \{\hat{\mathbf{x}}_2, \hat{\mathbf{y}}_2, \hat{\mathbf{z}}_2\}$ obtained from $\{l\}$ by a rotation about $\hat{\mathbf{y}}_l$ such that $\hat{\mathbf{z}}_l$ becomes backbone tangent at the end disk. Origin of $\{2\}$ is at center of the end disk.

- *End Disk Coordinate System* (EDS) $\{e\} \equiv \{\hat{\mathbf{x}}_e, \hat{\mathbf{y}}_e, \hat{\mathbf{z}}_e\}$ is fixed to the end disk. $\hat{\mathbf{x}}_e$ points from center to the 1*st* secondary backbone and $\hat{\mathbf{z}}_e$ is normal to the end disk. $\{e\}$ is obtained from $\{2\}$ by a rotation about $\hat{\mathbf{z}}_2$.

TABLE I
NOMENCLATURE USED IN THIS PAPER

m	Number of the secondary backbones
i	Index of the secondary backbones, $i = 1, 2, \cdots, m$
r_i	Distance from the virtual primary backbone to the i*th* secondary backbone.
β_i	β_i characterizes the division angle from the i*th* secondary backbone to the 1*st* secondary backbone. $\beta_l \equiv 0$ and β_i remain constant once the structure is built.
L, L_i	Lengths of the virtual primary and the i*th* secondary backbones measured from the base disk to the end disk.
d_i	Diameter of the i*th* secondary backbone
$\rho(s), \rho_i(s_i)$	Radius of curvature of the primary and the i*th* secondary backbones.
$\mathbf{q}$	$\mathbf{q} = [q_1 \ q_2 \ \cdots \ q_m]^T$ is the actuation lengths for the secondary backbones and $q_i \equiv L_i - L$.

| $\theta(s)$ | The angle of the tangent to the virtual primary backbone in the bending plane. $\theta(L)$ and $\theta(0)$ are designated by θ_L and θ_0, respectively. $\theta_0 = \pi/2$. |
δ_i	A right-handed rotation angle about $\hat{\mathbf{z}}_I$ from $\hat{\mathbf{x}}_I$ to a ray passing through the virtual primary backbone and the ith secondary backbone.
δ	$\delta \equiv \delta_I$ and $\delta_i = \delta + \beta_i$.
$\boldsymbol{\psi}$	$\boldsymbol{\psi} \equiv [\theta_L \quad \delta]^T$ defines the configuration of the structure.
$^b\mathbf{p}(s)$	Position vector of a point along the primary backbone in $\{b\}$. $^b\mathbf{p}(L)$ is the tip position and is designated by $^b\mathbf{p}_L$.
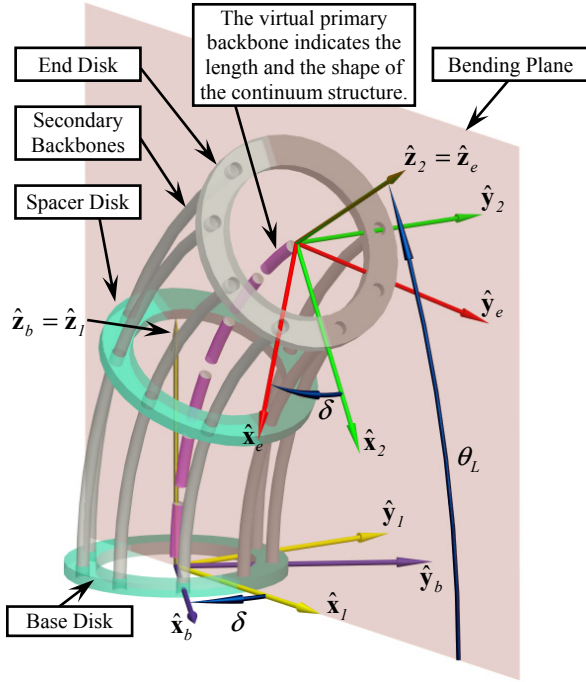
Fig. 3. Nomenclature and coordinates for a generic structure

B. Kinematics of Structure-I

Thorough kinematics analysis of Structure-I can be found in [16-18]. Related entities are summarized here which help the derivation of the kinematics of Structure-II and Structure-III.

Configuration of Structure-I is parameterized by $\boldsymbol{\psi}$ as defined in Table I. Projection of the ith secondary backbone on the bending plane is a curve which is offset by Δ_i from the primary backbone. $\rho_i(s)$ and $\rho(s)$ are related as follows:

$$\rho(s) = \rho_i(s_i) + \Delta_i \qquad (1)$$

Where $\Delta_i \equiv r_i \cos \delta_i = r_i \cos(\delta + \beta_i)$ and values of r_i and β_i for Structure-I are listed in Table II.

Length of the ith backbone can be obtained by an integral:

$$L_i = \int ds_i = \int (ds_i - ds + ds) = L + \int (ds_i - ds) \qquad (2)$$

Referring to Fig. 3, the integral above can be rewritten as in Eq. (3). Substituting Eq. (1) into Eq. (3) gives Eq.(4), which leads to the result as in Eq. (5):

$$\int (ds_i - ds) = \int_0^{\theta_0 - \theta_L} (\rho_i(s_i) - \rho(s)) d\theta \qquad (3)$$

$$\int_0^{\theta_0 - \theta_L} (\rho_i(s_i) - \rho(s)) d\theta = -\int_0^{\theta_0 - \theta_L} \Delta_i d\theta \qquad (4)$$

$$L_i = L - r_i \cos \delta_i (\theta_0 - \theta_L) = L + r_i \cos \delta_i (\theta_L - \theta_0) \qquad (5)$$

Referring to the definition of q_i in Table I, Eq. (5) gives:

$$q_i = r_i \cos \delta_i (\theta_L - \theta_0), \quad i = 1, 2, \cdots, m \qquad (6)$$

Rotation matrix $^b\mathbf{R}_e$ associates $\{e\}$ and $\{b\}$:

$$^b\mathbf{R}_e = \mathrm{R}(\hat{\mathbf{z}}_b, -\delta) \mathrm{R}(\hat{\mathbf{y}}_I, \theta_0 - \theta_L) \mathrm{R}(\hat{\mathbf{z}}_2, \delta) \qquad (7)$$

Where $\mathrm{R}(\hat{\mathbf{n}}, \gamma)$ designates rotation about $\hat{\mathbf{n}}$ by an angle γ.

Tip position of the continuum brace is given by:

$$^b\mathbf{p}_L = {}^b\mathbf{R}_I \left[\int_0^L \cos(\theta(s)) ds \quad 0 \quad \int_0^L \sin(\theta(s)) ds \right]^T \qquad (8)$$

Where $^b\mathbf{R}_I = \mathrm{R}(\hat{\mathbf{z}}_b, -\delta)$ and the integrals depend on the actual shape of the primary backbone.

When the shape of Structure-I is circular, Eq. (8) gives.

$$^b\mathbf{p}_L = \frac{L}{\theta_0 - \theta_L} \begin{bmatrix} \cos\delta(1 - \sin\theta_L) \\ \sin\delta(\sin\theta_L - 1) \\ \cos\theta_L \end{bmatrix} \qquad (9)$$

When θ_L approaches θ_0, Eq. (9) gives $^b\mathbf{p}_L = [0 \quad 0 \quad L]^T$.

C. Kinematics of Structure-II

There are 18 secondary backbones in Structure-II and the structural parameters are listed in Table II.

Redundant secondary backbones are added to improve the stiffness. Hence the differences between Structure-I and Structure-II only lie on the values of m, r_i and β_i.

Structure-II should also be actuated by pushing and pulling the secondary backbones according to the actuation length q_i as in Eq. (6), except that the correct values of m, r_i and β_i should be used.

The expressions of $^b\mathbf{R}_e$ and $^b\mathbf{p}_L$ remain the same as in Eq. (7) and Eq. (8).

D. Kinematics of Structure-III

The continuum components of Structure-III are identical to those of Structure-II, which are listed in Table II. A passive RRPRR rigid kinematic chain is integrated to further improve the torsional stiffness of the structure. Five additional configuration variables are hence introduced to describe the status of the RRPRR chain.

As shown in Fig. 4, besides BDS $\{b\}$ and EDS $\{e\}$, three additional coordinate systems ($\{r1\}$, $\{r2\}$ and $\{r3\}$) are assigned. Since $\{b\}$ and $\{e\}$ are assigned to describe the kinematics of the continuum manipulator, their attachment to the base and the end disks are not according to the Denavit–Hartenberg rules.

$\{b\}$ is related to $\{e\}$ through the following homogeneous transformations:

$$
{}^{b}\mathbf{T}_{r1} = \begin{bmatrix} s_{\phi_1} & c_{\phi_1} & 0 & 0 \\ 0 & 0 & 1 & 0 \\ c_{\phi_1} & -s_{\phi_1} & 0 & l_1 \\ 0 & 0 & 0 & 1 \end{bmatrix} \quad {}^{r1}\mathbf{T}_{r2} = \begin{bmatrix} c_{\phi_2} & -s_{\phi_2} & 0 & l_2 \\ 0 & 0 & 1 & 0 \\ -s_{\phi_2} & -c_{\phi_2} & 0 & 0 \\ 0 & 0 & 0 & 1 \end{bmatrix}
$$

$$
(10)
$$

$$
{}^{r2}\mathbf{T}_{r3} = \begin{bmatrix} c_{\phi_3} & -s_{\phi_3} & 0 & d_3 \\ s_{\phi_3} & c_{\phi_3} & 0 & 0 \\ 0 & 0 & 1 & 0 \\ 0 & 0 & 0 & 1 \end{bmatrix} \quad {}^{r3}\mathbf{T}_e = \begin{bmatrix} -s_{\phi_4} & 0 & c_{\phi_4} & l_4 + l_5 c_{\phi_4} \\ 0 & -1 & 0 & 0 \\ c_{\phi_4} & 0 & s_{\phi_4} & l_5 s_{\phi_4} \\ 0 & 0 & 0 & 1 \end{bmatrix}
$$

Where s_{ϕ_i} and c_{ϕ_i} are the sine and cosine functions of ϕ_i; ϕ_1, ϕ_2, ϕ_3, ϕ_4 and d_3 are passive configuration variables of this rigid RRPRR kinematic chain, depending on θ_L and δ; l_1, l_2, l_4 and l_5 are structural parameters.
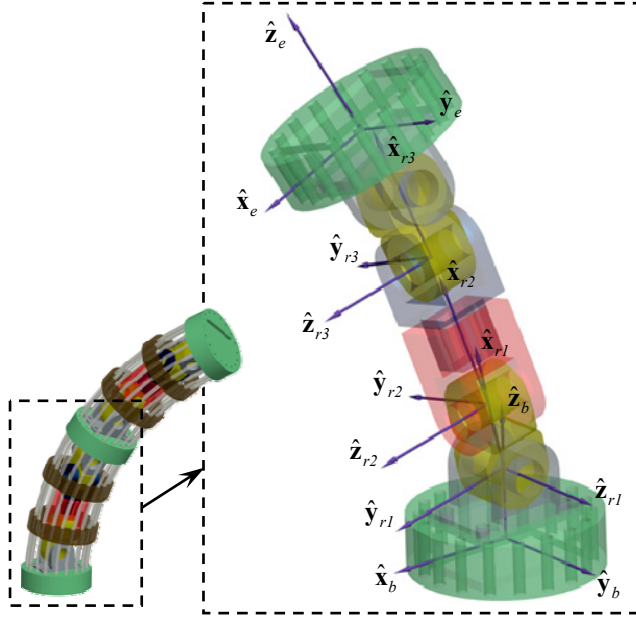

Fig. 4.   Additional coordinates for Structure-III

TABLE II
STRUCTURAL PARAMETERS OF THE TO-BE-COMPARED STRUCTURES

Structure-I	Structure-II and Structure-III		
$m = 3$	$m = 18$	$r_i = 3mm$	$d_i = 0.4mm$
$d_i = 0.4mm$	$r_i = 3mm$	$\beta_1 = 0,\ \beta_2 = \pi/9,\ \beta_3 = 2\pi/9,$	
$\beta_1 = 0,\ \beta_2 = 2\pi/3,\ \beta_3 = 4\pi/3$	$\cdots,\ \beta_{18} = 17\pi/9$		

IV.   IMPLEMENTATION OF A NOVEL ACTUATION SCHEME

When a structure similar to Structure-I was actuated in [16], three motorized lead screws are used to push and pull the secondary backbones, according to the actuation kinematics as in Eq. (6). However, using 18 motors to drive Structure-II and Structure-III doesn't seem smart when their push-pull actuation depends on only two variables (θ_L and δ).

A novel modular actuation scheme is hence introduced. Fig. 5(a) shows an extended continuum structure. It is formed as follows. A distal continuum structure is connected to a proximal continuum structure through a set of rigid guiding cannulae. The arrangement of the secondary backbones in the distal structure is scaled to that of the proximal structure. Bending of the proximal structure bends the distal structure in

the opposite way. Fig. 5(b) shows an actuation continuum structure. It could be bent by pushing and pulling four actuation backbones. The extended continuum structure could be assembled into the actuation continuum structure so that the actuation structure deforms the proximal structure so as to drive the distal structure, no matter how many backbones are there in the distal continuum structure.

This novel actuation scheme has a nice modular feature. Distal structures with different sizes can still be matched to the same proximal structure so that one actuation structure could drive many different distal structures.
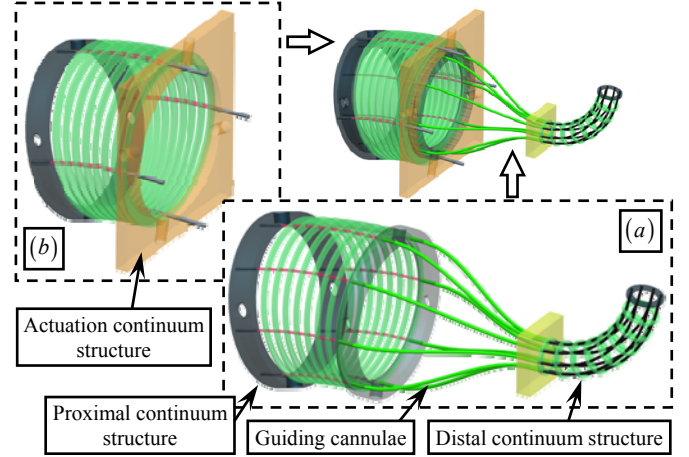

Fig. 5.   A novel module actuation scheme for all the structures: (a) an extended continuum structure and (b) an actuation continuum structure

The implemented actuation scheme is shown in Fig. 6. Four motorized ball screws push and pull four backbones of the actuation structure. A few sliding blocks prevent bulking of these backbones.
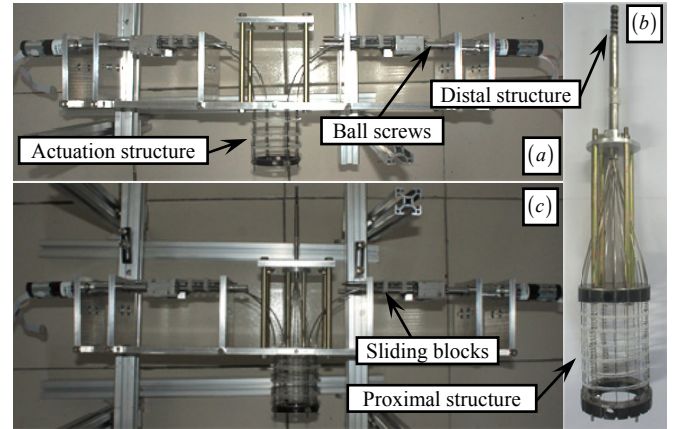

Fig. 6.   The implemented actuation scheme: (a) the actuation structure and (b) an extended structure can be assembled as shown in (c)

The four Maxon DC servomotors (A-max Ø16 with planetary gearhead) were controlled by a Matlab xPC Target to drive the ball screws according to the kinematics from Eq. (6) with correct r_i and β_i values substituted. Motion control cards included the D/A card PCL-727 from the AdvanTech Inc and the counter card CNT32-8M from the Contec Inc.

V.   EXPERIMENTAL CHARACTERIZATION

This paper seeks possible ways to enhance the stiffness of a

continuum manipulator while maintaining the simple presentation of its kinematics. Then a multi-DoF manipulator made from the stiffness-enhanced structures could be handily tele-operated while handling various payloads.

This section hence firstly presents a series of experiments, identifying the shapes of the structures. Results would show that Structure-II and Structure-III are still quite close to circular shapes and their kinematics can still be described by the kinematics as in Section III. Then the stiffness of the three structures will be quantified and compared in Section V.B.

A. Shape identification of the structures

A series of experiments were firstly conducted to identify the shapes of the three structures. The goal is to check whether the shapes of Structure-II and Structure-III are still close to circular arcs.

Each structure was bent to 4 configurations as listed in Table III. The actuation unit as in Fig. 6 was commended to push and pull the backbones for the actuated lengths according to the kinematics as in Eq. (6). Please be noted that Eq. (6) holds for the three to-be-compared structures as well as for the proximal continuum structure and the actuation continuum structure in the actuation unit shown in Fig. 5. The actual actuation lengths from the ball screws were converted according to the size ratio between the actuation continuum structure and Structure-I, Structure-II or Structure-III.

The shape identification process is based on an imaging process technique as detailed in [16, 17]. As shown in Fig. 7, after the surrounding pixels were manually erased, edges were then detected. All the points on the detected edges were used for curve fitting. Although the edge points from the background (or the internal structure) were not excluded, the shape identification errors would not be excessive since these points are approximately evenly distributed within the shape. Curve fitting results were overlaid back to the original picture to examine whether the fitted curves matched the shapes of the structures.

Using the curve fitting results, plots of bending angles versus curve lengths can be found in Fig. 8. Due to the definition of θ_L, the bending angle is equal to $90° - \theta_L$. Namely $\theta_L = -30°$ corresponds to a 120° bending, whereas $\theta_L = 60°$ corresponds to a 30° bending.

Results from Fig.8 showed that Structure-I and Structure-II bend to shapes very close to circular arcs. The results for Structure-I are consistent with previous results [16, 17].

Structure-III still has bending shapes close to circular arcs when the bending angles are relatively small. Its shapes differ from circular arcs when the total bending angle increases. The phenomenon is mainly due to the friction from the passive rigid kinematic chain inside. The bending performance of Structure-III can be improved by fabricating the parts of the rigid kinematic chain to tighter tolerances.

All the three structures bent less than the commanded bending angles. As shown in Fig. 8, when the structures were commanded to bend 120º ($\theta_L = -30°$), they only bent for

about 95º. This phenomenon is also consistent with previous results [19].

It should also be noted that the same amount of actuation led to slightly different bending of the three structures: Structure-I bent the most and Structure-III bent the least. Obviously the increase in the number of structural components from Structure-I to Structure-III caused more bending resistance. Bending of each structure could be individually calibrated and compensated as in [19].

TABLE III
BENDING CONFIGURATIONS FOR EXPERIMENTATION

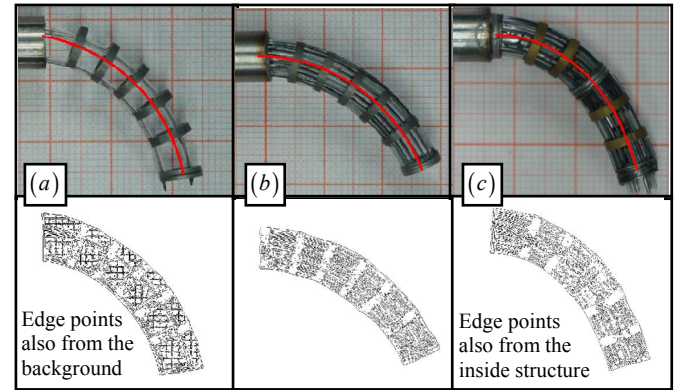| Configuration #1		Configuration #2	
$\delta = 0°$	$\theta_L = 60°$	$\delta = 0°$	$\theta_L = 30°$
Configuration #3		Configuration #4	
$\delta = 0°$	$\theta_L = 0°$	$\delta = 0°$	$\theta_L = -30°$

Fig. 7. Image processing & curve fitting for shape identification: (a) Structure-I, (b) Structure-II, and (c) Structure-III
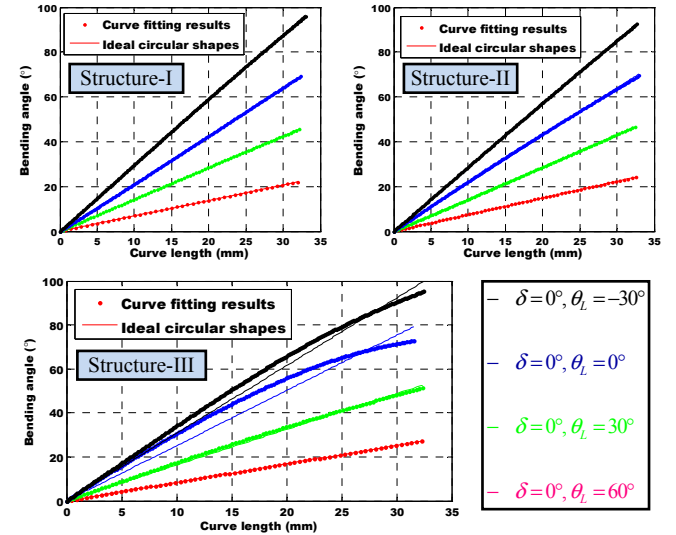

Fig. 8. Bending angles of the structures along their lengths

B. Stiffness characterization of the structures

The stiffness properties of the three structures is quantified and compared in this section.

The experimental setup is shown in Fig. 9. A 3D force sensor (K3D60 from ME-Meßsysteme GmbH) with a probe attached is carried by a XYZ motion stage. The measurement ranges of the 3D force sensor are all ±50N in the XYZ directions. The sensor was connected to a DAQ card (Advantech PCL-818HG) and a sensing accuracy of 0.04 N

was achieved.

The continuum structures were either at their straight configurations or bent to a configuration listed in Table III. The XYZ motion stage firstly moved the probe to start touching the tip of the continuum structure. Then the structure was perturbed for a few millimeters in XYZ directions and the reaction forces were recorded by the force sensor. The stiffness was calculated as the reaction force divided by the deflection distance (perturbation distance). This approach of quantifying stiffness was also practiced in [17].
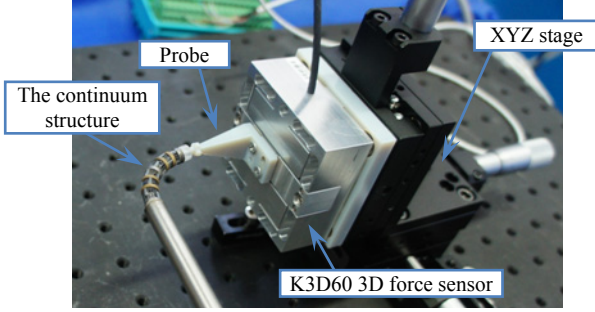

Fig. 9.   Experimental setup for stiffness characterization

The forces were measured with respect to the tip deflection for the three structures under straight configurations and the configuration listed in Table III.

Figure 10 plots the force versus the deflection in the $\hat{\mathbf{x}}_b$ and $\hat{\mathbf{y}}_b$ directions for the three structures under configuration #4 ($\delta = 0°, \theta_L = -30°$). A slope can be fitted to the measurements to estimate the stiffness of the structures in both $\hat{\mathbf{x}}_b$ and $\hat{\mathbf{y}}_b$ directions under this specific configuration.
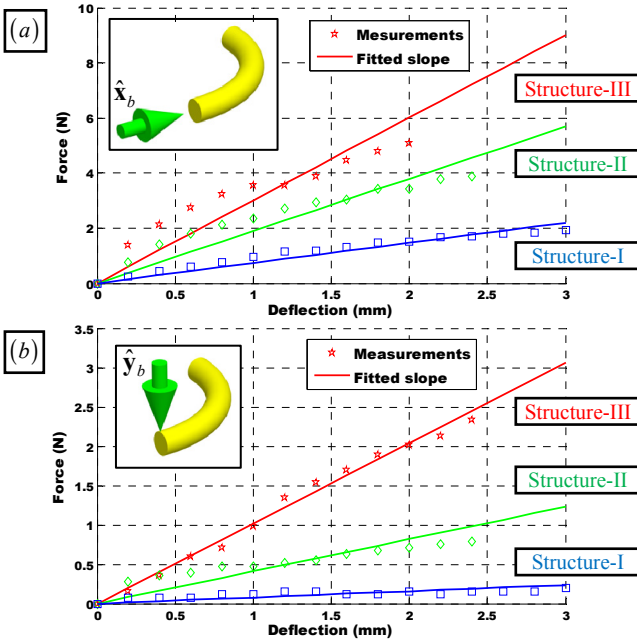

Fig. 10.   The force versus the deflection for the structures in (a) $\hat{\mathbf{x}}_b$ and (b) $\hat{\mathbf{y}}_b$ directions under configuration $\delta = 0°, \theta_L = -30°$

The estimated stiffness values of each structure in the $\hat{\mathbf{x}}_b$ and $\hat{\mathbf{y}}_b$ directions are plotted with respect to the commanded bending angles in Fig. 11.

From the results in Fig. 11, one can make the following observations.

- Structure-III has a higher stiffness than Structure-II due to the presentence of the passive rigid kinematic chain.
- Structure-II has 18 backbones while Structure-I only has 3 backbones. It's understandable that Structure-II has a higher stiffness. But the stiffness is only about 3 to 4 times higher. This means when more backbones are included, they don't contribute equally and the stiffness doesn't increase linearly.
- When the commanded bending angle is 0º (in a straight configuration), the Structure-II's stiffness in the $\hat{\mathbf{x}}_b$ direction is similar to that in the $\hat{\mathbf{y}}_b$ direction due to the structure symmetry. The Structure-III's stiffness in the $\hat{\mathbf{x}}_b$ direction is higher than that in the $\hat{\mathbf{y}}_b$ direction due to the non-symmetrical structure of the passive kinematic chain.
- When the commanded bending angel increases, the structures' stiffness in the $\hat{\mathbf{x}}_b$ direction all increase. The reason could be qualitatively explained. When an external perturbation is applied to the tip, the structure deflects and the external perturbation does positive work to increase the elastic potential energy of the structure. If the original system energy is higher, the structure might deflect less for the same perturbation because the same small amount of energy input would generate a smaller shape variation.
- On the other hand, the stiffness of Structure-I and Structure-II in the $\hat{\mathbf{y}}_b$ direction decreases when the structures bend more. This is because the perturbation at the tip in the $\hat{\mathbf{y}}_b$ direction exerts a torque at the structures' base. The low torsional stiffness of the two structures leads to low translational stiffness at the tip in the $\hat{\mathbf{y}}_b$ direction. The rigid kinematic chain in Structure-III is integrated to improve the torsional rigidity. The enhanced torsional rigidity results in the improved translational stiffness at the tip of Structure-III.

According to the stiffness values of Structure-III, if it is implemented in a surgical robot to manipulate a payload of 2N, the distal deflection would be about 0.7 to 2.5mm.

VI. CONCLUSION AND FUTURE WORK

Continuum structures become popular in medical systems due to i) their intrinsic compliance for safe interactions and/or ii) the design compactness for distal dexterity achieved by stacking multiple segments and streaming actuation from a proximal unit to the distal end.

Continuum manipulators are sometimes expected to have relatively high stiffness to handle payloads in robotic surgeries. This paper hence explores how to enhance the stiffness properties by presenting an experimental kinestatic study between three different continuum manipulators. The objective is to maintain simple circular shapes for the bent continuum segments but to improve the stiffness properties.

The addition of more backbones is enabled by the introduction of a novel modular actuation scheme. What's more, a passive rigid kinematic chain is integrated to further

improve the stiffness. The RRPRR chain from this paper is designed for better torsional rigidity. With more backbones plus and a rigid kinematic chain, the translational stiffness of Structure-III is now 5 to 6 times better than that of Structure-I.

Results of this paper also open a few topics for future studies. An elasticity model is needed to reveal the changes in stiffness with respect to the changes in the number of backbones. Then the optimal number of backbones could be determined. Moreover, further understanding is also greatly needed on how to design a hybrid continuum-rigid manipulator for better or controllable stiffness properties.
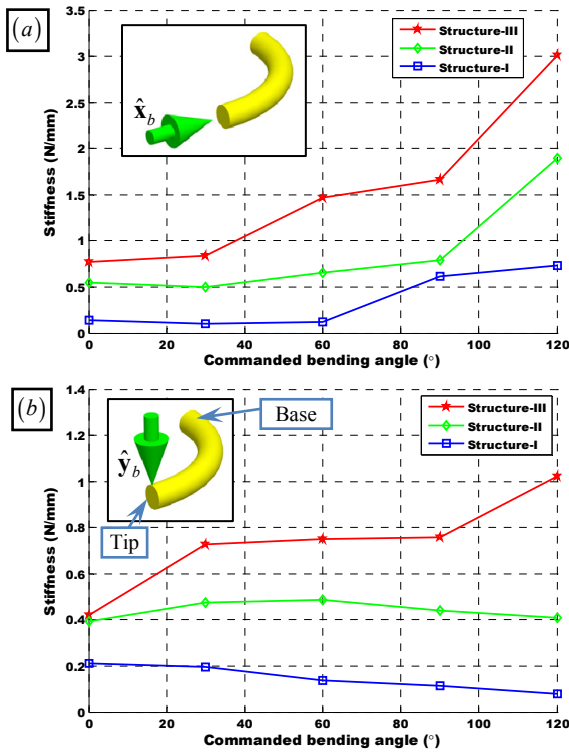

Fig. 11. Stiffness versus commanded bending angle in (a) $\hat{\mathbf{x}}_b$ and (b) $\hat{\mathbf{y}}_b$ directions

REFERENCES

[1] G. Robinson and J. B. Davies, "Continuum Robots - A State of the Art," in *IEEE International Conference on Robotics and Automation (ICRA)*, Detroit, Michigan, 1999, pp. 2849-2853.

[2] K. Suzumori, S. Iikura, and H. Tanaka, "Applying a Flexible Microactuator to Robotic Mechanisms," *IEEE Control Systems Magazine,* vol. 12, No.1, pp. 21-27, Feb 1992.

[3] S. Hirose, *Biologically Inspired Robots, Snake-Like Locomotors and Manipulators*: Oxford University Press, 1993.

[4] D. M. Lane, J. B. C. Davies, G. Casalino, G. Bartolini, G. Cannata, G. Veruggio, M. Canals, C. Smith, D. J. O'Brien, M. Pickett, G. Robinson, D. Jones, E. Scott, A. Ferrara, D. Angelleti, M. Coccoli, R. Bono, P. Virgili, R. Pallas, and E. Gracia, "AMADEUS: Advanced Manipulation for Deep Underwater Sampling," *IEEE Robotics & Automation Magazine,* vol. 4, No.4, pp. 34-45, Dec 1997.

[5] W. McMahan, V. Chitrakaran, M. Csencsits, D. M. Dawson, I. D. Walker, B. A. Jones, M. Pritts, D. Dienno, M. Grissom, and C. D. Rahn, "Field Trials and Testing of the OctArm Continuum Manipulator," in *IEEE International Conference on Advanced Robotics (ICAR)*, Orlando, FL, USA, 2006, pp. 2336-2341.

[6] P. E. Dupont, J. Lock, B. Itkowitz, and E. Butler, "Design and Control of Concentric-Tube Robots," *IEEE Transactions on Robotics,* vol. 26, No.2, pp. 209-225, April 2010.

[7] J. Burgner, P. J. Swaney, T. L. Bruns, M. S. Clark, D. C. Rucker, E. C. Burdette, and R. J. Webster, "An Autoclavable Steerable Cannula Manual Deployment Device: Design and Accuracy Analysis," *Journal of Medical Devices,* vol. 6, No.041007, pp. 1-7, Dec 2012.

[8] Y. Haga, M. Esashi, and S. Maeda, "Bending, Torsional and Extending Active Catheter Assembled Using Electroplating," in *International Conference on Micro Electro Mechanical Systems (MEMS)*, Miyazaki, Japan, 2000, pp. 181-186.

[9] D. B. Camarillo, C. R. Carlson, and J. K. Salisbury, "Configuration Tracking for Continuum Manipulators With Coupled Tendon Drive," *IEEE Transactions on Robotics,* vol. 25, No.4, pp. 798-808, Aug 2009.

[10] K. Ikuta, Y. Matsuda, D. Yajima, and Y. Ota, "Pressure Pulse Drive: A Control Method for the Precise Bending of Hydraulic Active Catheters," *IEEE/ASME Transactions on Mechatronics,* vol. 17, No.5, pp. 876-883, Oct 2012.

[11] P. Dario, C. Paggetti, N. Troisfontaine, E. Papa, T. Ciucci, M. C. Carrozza, and M. Marcacci, "A Miniature Steerable End-Effector for Application in an Integrated System for Computer-Assisted Arthroscopy," in *IEEE International Conference on Robotics and Automation (ICRA)*, Albuquerque, NM, USA, 1997, pp. 1573-1579.

[12] V. K. Asari, S. Kumar, and I. M. Kassim, "A Fully Autonomous Microrobotic Endoscopy System," *Journal of Intelligent and Robotic Systems,* vol. 28, No.4, pp. 325-341, Aug 2000.

[13] N. Simaan, K. Xu, A. Kapoor, W. Wei, P. Kazanzides, P. Flint, and R. H. Taylor, "Design and Integration of a Telerobotic System for Minimally Invasive Surgery of the Throat " *International Journal of Robotics Research,* vol. 28, No.9, pp. 1134-1153, 2009.

[14] J. Ding, R. E. Goldman, K. Xu, P. K. Allen, D. L. Fowler, and N. Simaan, "Design and Coordination Kinematics of an Insertable Robotic Effectors Platform for Single-Port Access Surgery," *IEEE/ASME Transactions on Mechatronics,* vol. 18, No.5, pp. 1612-1624, Oct 2013.

[15] J. Zhao, X. Zheng, M. Zheng, A. J. Shih, and K. Xu, "An Endoscopic Continuum Testbed for Finalizing System Characteristics of a Surgical Robot for NOTES Procedures," in *IEEE/ASME International Conference on Advanced Intelligent Mechatronics (AIM)*, Wollongong, Australia, 2013, pp. 63-70.

[16] K. Xu and N. Simaan, "Analytic Formulation for the Kinematics, Statics and Shape Restoration of Multibackbone Continuum Robots via Elliptic Integrals," *Journal of Mechanisms and Robotics,* vol. 2, Feb 2010.

[17] K. Xu and N. Simaan, "An Investigation of the Intrinsic Force Sensing Capabilities of Continuum Robots," *IEEE Transactions on Robotics,* vol. 24, No.3, pp. 576-587, June 2008.

[18] R. J. Webster and B. A. Jones, "Design and Kinematic Modeling of Constant Curvature Continuum Robots: A Review " *International Journal of Robotics Research,* vol. 29, No.13, pp. 1661-1683, Nov 2010.

[19] K. Xu and N. Simaan, "Actuation Compensation for Flexible Surgical Snake-like Robots with Redundant Remote Actuation," in *IEEE International Conference on Robotics and Automation (ICRA)*, Orlando, Florida, USA, 2006, pp. 4148-4154.